Triggered Fault Slip by the 2017 Mw 7.3 Iran-Iraq Earthquake

Bennett Kellmayer

Date: 4/25/2023

Advisor: Mong-Han Huang

GEOL394

Abstract:

Earthquakes are a well-known hazard to people living in seismically active areas of the world. However, new evidence suggests that earthquakes can trigger fault slip and possibly generate more and smaller earthquakes to occur at distance. This is because of the release of energy and the increase of dynamic or static Coulomb stress on the receiver faults can potentially trigger these faults to slip. In this study, interferometric synthetic aperture radar (InSAR) is used to investigate shallow slip on faults that are likely to be triggered by the 2017 Mw 7.3 Iran-Iraq earthquake was investigated. The study found that, in addition to faulting parallel to the slip event, a faulting pattern occurring nearly perpendicular to the coseismic slip of the fault was observed, primarily located southeast of the epicenter. Further analysis revealed that the fault in this area was strengthened against slip by the coseismic static Coulomb stress change. The ground displacement in 150 km radius around the earthquake's epicenter was simulated to calculate the peak dynamic Coulomb stress. To examine this, the velocity and acceleration that the ground felt as a result of the main shock was modeled using ground displacement data. These models allowed for spatial analysis the ephemeral effects of the main shock's propagation to understand exactly how this rupture occurred. The results showed a correlation between the location of higher dynamic Coulomb stress change and the observed slips. This correlation with the triggering mechanism of the additional slip having been the dynamic Coulomb stress change imposed by the fault than the associated static Coulomb stress change.

Plain-Text Summary:

Natural disasters account for many deaths worldwide every year. Events such as landslides, hurricanes, and earthquakes are constantly being studied for many purposes and this research can be lifesaving for some. In recent years satellite imaging has become very prevalent in the study of these events with techniques such as Interferometric Synthetic Aperture Radar (InSAR) being an invaluable asset. This technique allows researchers to see very small changes in the ground over time which has allowed better constraints on ground motion caused by earthquakes. This study in particular investigated how the 2017 Mw 7.3 Iran-Iraq earthquake caused additional faults to slip in the area around the main fault. To examine this the net difference in the levels of stress that the ground felt, known as the static stress was modeled. This was compared to dynamic stress, which is a measure of how much force the ground felt in an instant. These were then mapped against the areas identified as fault slip from InSAR observations to see how these different processes matched with the observations. The model showed a stronger correlation with the more variable dynamic stress from which suggests that the dynamic model was more likely to be what caused the observed slip.

1 Introduction & Background:

The Zagros Mountains of western Iran are a major source of seismic activity in the world. The orogen associated with this mountain range is the site of the collision between the Eurasian and Arabian plates as is shown in figure 1. The collision of these plates formed a fold-and-thrust belt on the western side of the range. The Zagros fold-and-thrust belt is unusual for continental collisions because all earthquake coseismic slip previously documented in the region are along blind faults, meaning that there are no surface ruptures (Nissen et al., 2016). Despite this the

Zagros Mountains range is one of the most seismically active regions in the world resulting in many large slip events (Barnhart et al. 2018).

Figure 1: Map of earthquake region from ESRI. The epicenter is marked with a black star and the major plate boundaries are marked with red lines (ESRI, 2011).

There was a powerful earthquake of Mw 7.3, that struck this region on November 12, 2017, near the town of Darbandikhan, Iraq. This devastating event killed more than 630 people and injured thousands more. While there was destruction across the region most of the damage came from building collapses and landslides, and there was no surface rupture identified with the event.

Remote sensing has become popular in earthquake studies because it, allows researchers to quickly access surface displacement data and observe events across the world and in difficult to reach places. In particular, technology such as Synthetic Aperture Radar (SAR) is a key tool for geophysical analysis in the modern era. This technique is particularly essential when in-situ measurements such as GPS data in such regions as Iran and Iraq are absent. Spaceborne repeat-pass systems allow researchers to compare the radar phase difference between two or more acquisitions. This is known as SAR Interferometry or InSAR and this method can be used to create maps of deformation down to the scale of a few millimeters to one centimeter (Simons and Rosen, 2015). InSAR is a very efficient method for determining things such as slip orientation and how widespread the damage is.

InSAR analysis, however, cannot capture the direction of motion along a fault because it measures static displacement. Therefore, seismic data are still needed to determine the hypocenter location relative to the slip area and thereby determine the directivity of the slip. As earthquake slip occurs over a finite plane, with a distinct starting point and distinct point of arrest, there is a direction of propagation of the fault slip. This directivity is important for understanding how the seismic waves from the rupture propagate. This directivity is crucial to knowing how the Coulomb stress is present in the system as a result of the fault. Simply put, the

directivity of the slip governs how quickly an individual point on the ground feels the entire force of the seismic waves released by the slip.

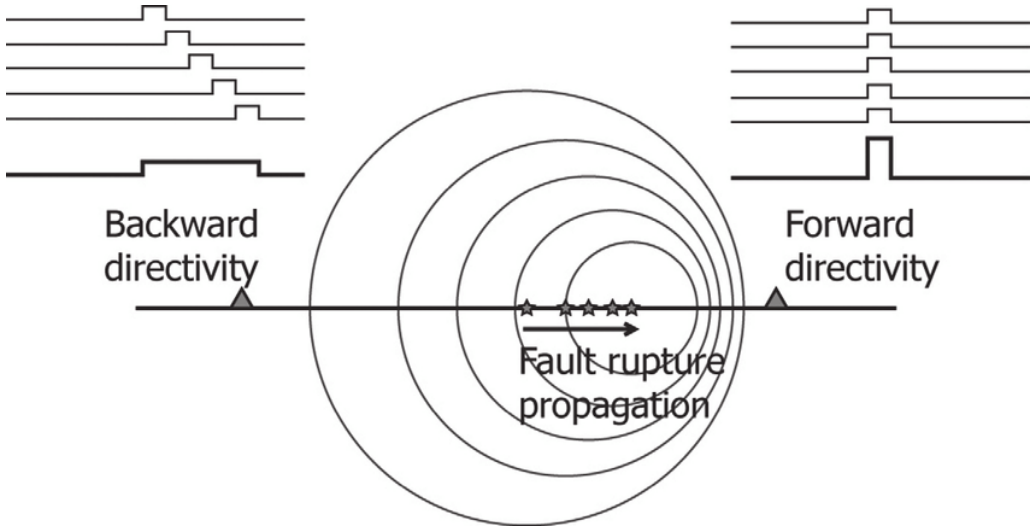

Figure 2: Model of seismic wave propagation due to fault directivity. Taken from Grimaz and Malisan (2014).

Figure 2 shows a simplified example of how directivity affects propagation. The effect produces a much higher intensity of energy release in a short amount of time in the forward direction. Whereas in the backwards direction the same amount of energy is propagating through the system, but it is spread out over a much longer time frame. This results in the forward direction feeling much more of the effect of both body and surface waves, as the maximum intensity is much higher. The difference in effect based on direction will also contribute to the difference between how much static and dynamic Coulomb stress change that various parts of the system will experience.

1.1 SAR Interferometry:

SAR Interferometry is a relatively new technique to image the surface of the earth. With the first major satellite ERS, having been launched by the European Space Agency in the summer of 1991 (Attema et al. 1998). Shortly after being launched ERS was able to analyze the Landers earthquake in 1992, showing the world the ingenuity of this satellite and the data processing methods (Massonnet et al. 1993). Given SAR signals operate in the microwave range these systems can image equally well at day and night and are not limited by cloud cover such as with optical observations (Simons and Rosen, 2015). Traditionally radar systems have a resolution governed by the length of their antenna and their distance from the object they are observing. Given the altitude of SAR satellites the resolution of a pixel, the smallest resolvable element for SAR analysis, within the image would only be able to be 5-10 km of area on the surface and therefore be almost useless to understanding small scale deformation (Bürgmann et al., 2000). In order to achieve high resolutions using these systems, the satellite uses information about its orbital pattern as well as more advanced signal processing techniques to achieve much higher resolution images. This allows the signal to be processed as though the antenna was

kilometers long despite only being a few meters long (Simons and Rosen, 2015). A simple configuration of a typical SAR system is shown in figure 3.

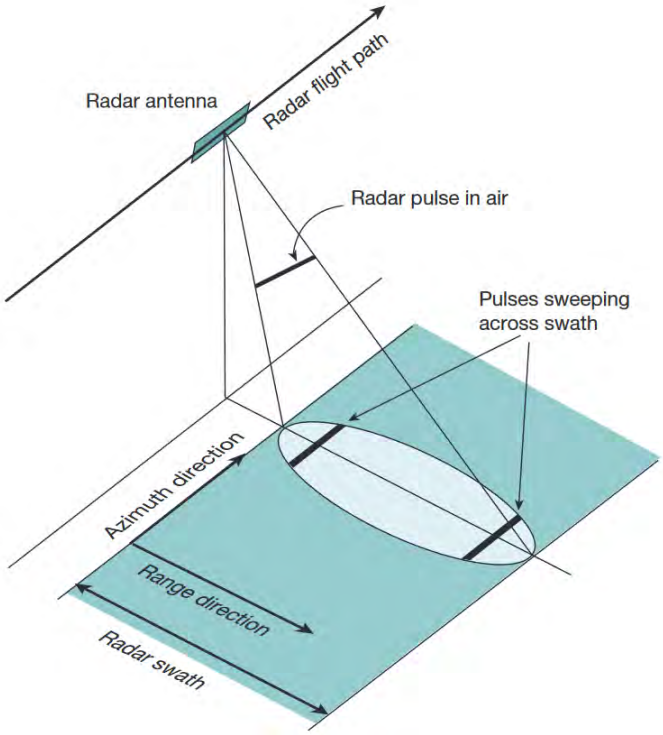

Figure 3: Typical SAR Imaging Scenario taken from Simons and Rosen (2015). The satellite flies forward in the azimuth direction, with the range direction being perpendicular to it. As the satellite flies over the target area, it images a finite width in the range direction which creates the swath.

This setup, however, has an inherent drawback in that the elevation change it reads is in terms of the line-of-sight direction of the radar pulse. Coupled with this, the line-of-sight must be angled forward to synthesize the larger aperture desired for the high resolution. Because the radar pulse is creating a two-dimensional image from a three-dimensional source all changes in the line-of-sight direction will be recorded as elevation change (Simons and Rosen., 2015).

SAR interferometry takes the difference of the phase value of each pixel between two SAR images and combines them creating an interferogram, allowing researchers to interpret differences in elevation of the target between these acquisitions (Bürgmann et al., 2000). Using a series of captures distributed temporally, typically referred to as a repeat-pass system, a time-series of deformation can be created. More recent systems such as Sentinel-1 and the upcoming NISAR mission have a repeat time of 12 days, a significant reduction in repeat time than previous systems such as ERS (Das et al., 2021).

In order to compare these acquisitions, NASA's Jet Propulsion Lab (JPL) developed the ISCE-framework which analyzes the phase difference of the returning radar waves (Gurrola et al., 2016). The interferometric phase (Φ) is (Rosen et al., 2000).

$$\Phi = \frac{4\pi\rho_1}{\lambda}\left[\left(1 - 2\left(\vec{B}\cdot\hat{l}_1\right)/\rho_1 + \left(B/\rho_1\right)^2\right)^2 - 1\right]. \quad (1)$$

where ρ_1 is the distance the radar wave travels during the first acquisition, λ is the wavelength of light emitted by the satellite, $\hat{l}_1$ is the unit vector in the range direction, B is the baseline separation, and $\vec{B}$ is the baseline vector. Given that in modern applications the baseline vector is much smaller than the ray path vector, the phase can be approximated as (Zebker & Goldstein, 1986).

$$\phi \approx -4\frac{\pi}{\lambda} \cdot B \cdot \sin(\theta - \alpha). \quad (2)$$

Where α represents the depression angle of an illuminated point on the surface. This relation allows for the creation of an interference pattern based on the phase difference between the two images and maps it from 0 to 2π in what is known as a wrapped interferogram. This cyclicity expresses itself as fringes on the interferogram. These fringes will show stark discontinuities at areas with significant motion on the surface and thereby signaling likely areas of surface rupture as shown in figure 4.

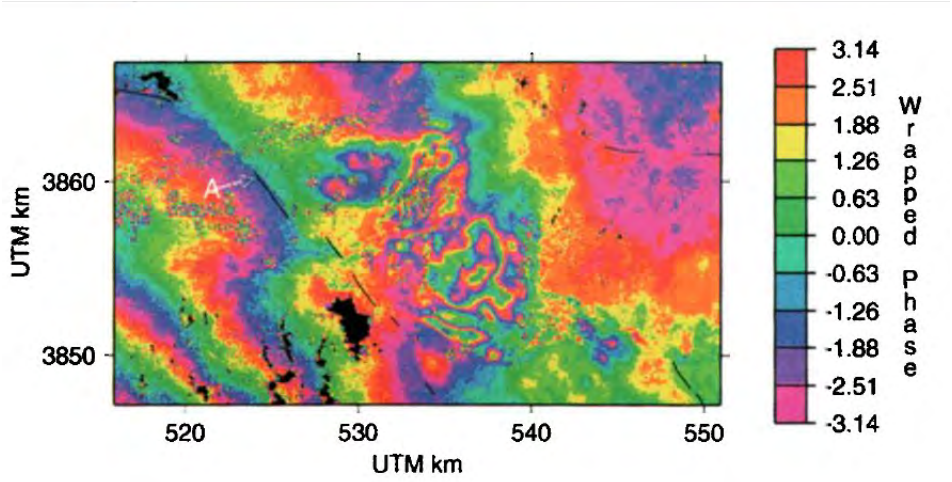

Figure 4: InSAR map of small-scale deformation related to the Landers, California, earthquake in 1992, taken from Price & Sandwell 1998.

The Sentinel-1 satellite employs a collection method known as terrain observation by progressive scan (TOPS) in order to increase the accuracy of SAR acquisitions. The TOPS system breaks the target area into three "sub-swaths" which are scanned separately and coregistered together resulting in resolutions accuracies better than 0.001 of a pixel in the azimuth direction (Fattahi et al., 2017) Uncertainty of the acquisitions, therefore, comes from misregistration in the azimuth direction. This uncertainty in the azimuth direction is equivalent to 1.6-2.8 cm of orbital uncertainty in the azimuth direction (Fattahi et al., 2017). For TOPS data collection orbital uncertainty is the cause of constant azimuth misregistration and thereby the main constraint on the overall uncertainty in the system (Fattahi et al., 2017).

1.2 Coulomb Stress:

Earth's crust is always subject to stress in multiple directions. These stresses typically hold the surface in a homeostatic equilibrium allowing only small amounts of motion. However, events such as earthquakes and landslides cause these stresses to spatially redistribute and result in different areas of the crust strengthening and weakening. This can be represented as the

Coulomb stress criterion which says that failure occurs when the Coulomb stress ($\Delta\sigma_f$) exceeds a certain value (King et al., 1994)

$$\Delta\sigma_f = \Delta\tau_\beta - \mu(\Delta\sigma_\beta - p). \quad (3)$$

where $\Delta\tau_\beta$ is the change in shear stress, $\Delta\sigma_\beta$is the change in normal stress, p is the pore fluid pressure, and μ is the friction coefficient. This relationship makes the Coulomb stress criterion a valuable proxy for crustal stability as stress changes greater than $\Delta\sigma_f$ will either advance the failure of future earthquakes or generate new instabilities in the rock (Kilb et al., 2002). Coulomb stress failure comes in two forms. First, static Coulomb stress change is the permanent net stress change from an event is what is used to determine areas of strengthening and weakening and considers only the static displacement (Kilb et al., 2002). In order to analyze static Coulomb stress change, seismologists define the geometry of the event using a source fault, which experiences slip, and a receiver which typically does not. After an earthquake if the Coulomb stress increases in a certain area, then that portion of the crust is said to become less stable, and for areas where the Coulomb stress decreases, they are said to have become more stable. In this case a key control on which regions strengthen and which weaken is the ratio of the change in shear stress relative to the change in normal stress. Two different endmember idealized stress change fields after a strike-slip earthquake, as shown in figure 5, to emphasize this difference (King et al., 1994)

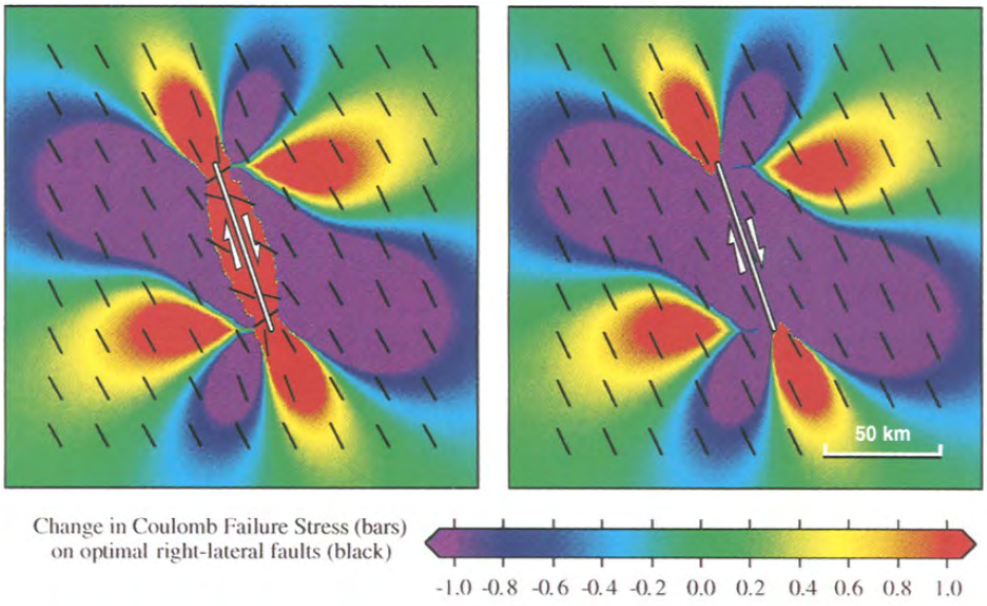

Figure 5: Idealized stress change as a result of a strike slip fault, taken from King et al., (1994). The left image shows a shear to normal stress change ratio of 1:1 whereas the right image shows a shear to normal stress change ratio of 1:10.

While static Coulomb stress change is relatively easy to model, dynamic Coulomb stress change is more difficult because the effects generated are more ephemeral. The dynamic form of Coulomb stress change considers the maximum change in stress that a receiver fault experiences during an event as a result of the propagation of seismic waves. Figure 6 below shows an

depiction of the difference between static and dynamic Coulomb stress change (Yoshida et al. 2020).

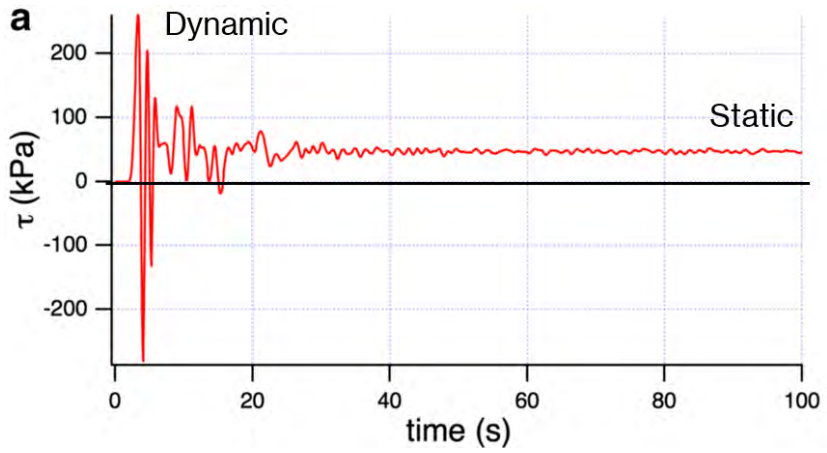

Figure 6: Depiction of the difference between dynamic Coulomb stress change, represented by the peak values on the stress vs time graph. Conversely, the static Coulomb stress change is represented by the difference between the final and initial stress values.

Dynamic Coulomb stress change is where the directivity of the fault plays into the problem, with the direction of propagation feeling a much more intense shock pattern than the opposite direction. Because of this the impacts of the dynamic stress change, induced by seismic wave propagation can be both more intense and cover a wider area (Kilb et al., 2002). Figure 6 shows an example of the intensity difference between the static and dynamic Coulomb stress change, that arose as a result of the Kaikoura, New Zealand earthquake in 2017 (Wallace et al. 2017)

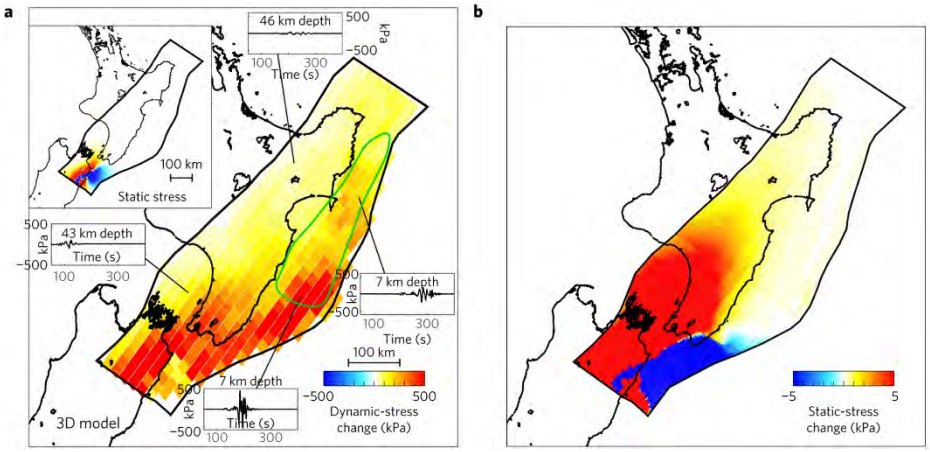

*Figure 7: Characterization of the difference between dynamic and static stress change from Wallace 2017. (**a**) shows the resultant dynamic Coulomb stress change from -500 kPa to 500 kPa. (**b**) shows the resultant static Coulomb stress change -5 kPa to 5 kPa.*

The dynamic Coulomb stress change, observed during the Kaikoura, New Zealand earthquake was nearly 1,000 greater than the static Coulomb stress change at various locations. It is believed that in this case the greater dynamic Coulomb stress change triggered a slow slip

event in the area. Therefore, in order to understand how the stress conditions of a fault are evolving looking at the static and dynamic stress conditions are very important. It is theorized that stress change is the driving force for successive earthquake triggering events, therefore this study has placed a large emphasis on the interplay of these stresses.

1.3 Triggered Fault Slip

Recently many seismologists have been interested in exploring how earthquakes trigger other seismic events. For instance, a recent study explored the triggering effect of the M_w 7.0 Harnai earthquake in Pakistan that occurred in 1997 on an associated M_w 6.8 aftershock that occurred 19 seconds later (Nissen et al., 2016). The data analyzed in this study showed that the Harnai, Pakistan earthquake was a doublet in which the first slip triggered the second. Another recent investigation of triggered fault slip utilized rigorous modeling techniques to learn that larger earthquakes preferentially trigger other larger events (Nandan et al. 2022).

2 Objectives:

This study asks: Whether if earthquakes can trigger slip on other faults, and if so, how? To evaluate this question, the 2017 Mw 7.3 Iran-Iraq earthquake was selected in order to examine the interplay of static and dynamic stresses in the system. When examining this event using InSAR there were a large number of smaller slip events oriented almost perpendicular to the slip on the main shock. These slip events were primarily located in the southeast portion of the study region as shown in figures 8 and 9.

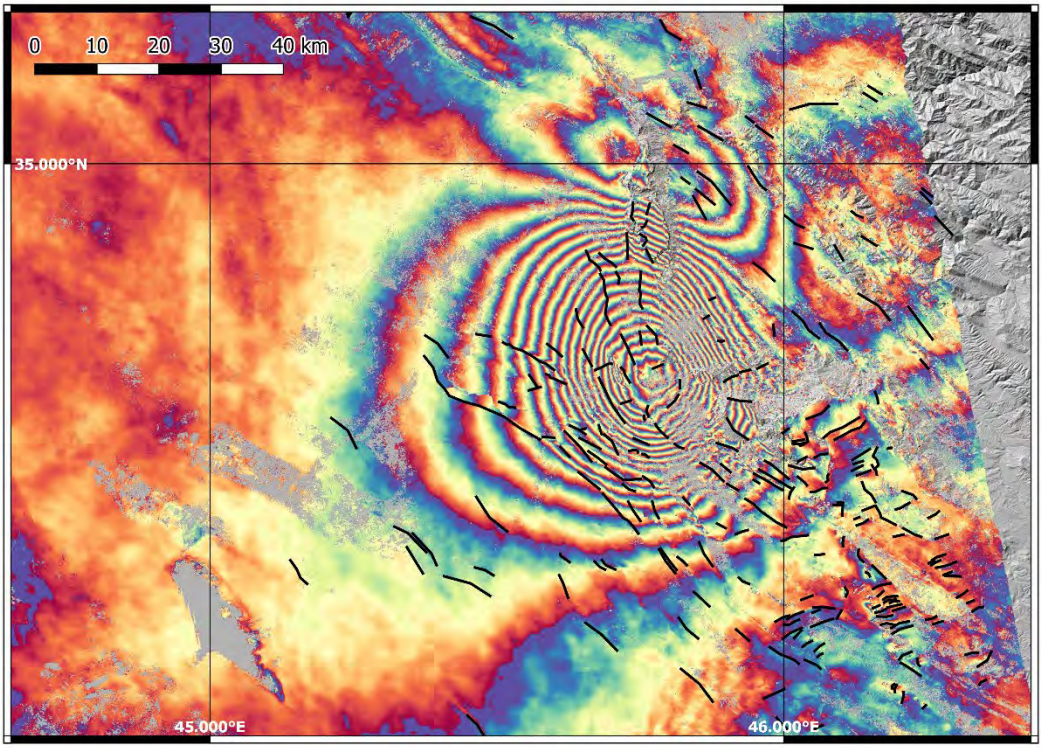

Figure 8: Coseismic interferogram of the 2017 M_w 7.3 Iran-Iraq Earthquake with notable surface deformation marked with black lines.

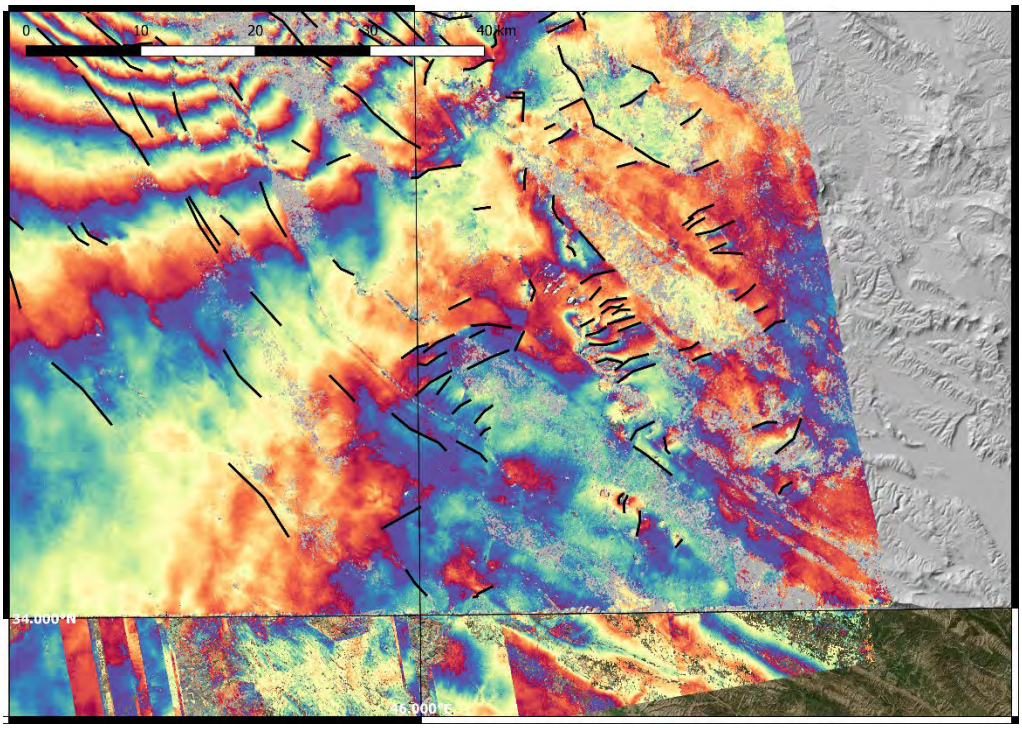

Figure 9: InSAR map from Figure 7, focused on the area of interest.

Figures 8 and 9 show the data acquired from studying the region with InSAR. Areas of instantaneous changes in the phase, as opposed to a smooth transition, was considered to be ground motion. The triggered slip was mapped using QGIS 3.4 and were identified by linear features where the phase jumps instead of transitioning continuously. While not every point of observed ground motion is guaranteed to be triggered slip, the linear nature of the features as well as the proximity to a major earthquake indicate that these areas are most likely slip induced by the main shock. The specific slip planes marked on the map are primarily a demonstrative measure. Black lines are included in figures 8 and 9 denoting where many of the observed slips were identified. Even with the addition of human error however, it is plain to see a greater frequency of these fractures in the southeastern portion of the map. In addition to the presence of these features being present, there was an interesting clustering pattern observed to the southeast of the hypocenter. This observation led to a desire to understand the directivity associated with the main shock of the earthquake, as that is the most likely cause for this asymmetry in distribution.

3 Hypothesis:

This null hypothesis of this study was that there was no discernable connection between the Coulomb stress change of the region as a result of the 2017 M_w 7.3 Iran-Iraq earthquake and the triggered slip identified earlier. In addition to this there were two alternative hypotheses tested as a part of this study. The first alternative hypothesis stated that there is a discernable connection between the static Coulomb stress change of the main shock and the triggered slip. The second alternative hypothesis stated that there is a discernable connection between the dynamic Coulomb stress change of the main shock and the triggered slip.

To explore these hypotheses further the static Coulomb stress change was calculated and plotted spatially against the triggered slip events. To examine the dynamic coulomb stress change as a result of the main shock, the propagation of the earthquake was modeled using finite fault inversion and synthetic seismograms.

4 Data and Methods:

4.1 Static Coulomb Stress Change Analysis

In order to evaluate whether deformation was driven by the static Coulomb stress change or the dynamic stress change from the earthquake, several programs were employed in order to model the event. To calculate the static Coulomb stress, change the Coulomb 3.3 program from USGS as well as their Finite Fault Inversion data were utilized (Toda et al., 2011). The data were then mapped using QGIS in order to spatially analyze the outputs received and correlate results with each other.

Finite Fault Inversion attempts to reconstruct the way that the fault slipped by inverting the body and surface waves produced by the event. The USGS uses the seismic moment of the event as well as the shear modulus of the surrounding rock to estimate the slip along the fault plane. The shear modulus of the study area is estimated to be 30 GPa (Wang and Bürgmann, 2020). This process is known as Finite Fault Inversion, and it produces a stress change map based on a given strike and dip of the fault plane. The strike and dip are given by the moment tensor of the fault, which in this case are 354.0° and 16.0°, respectively. The amplitude of slip is then plotted on a color scale imposed over a spatial distribution as shown in figure 10.

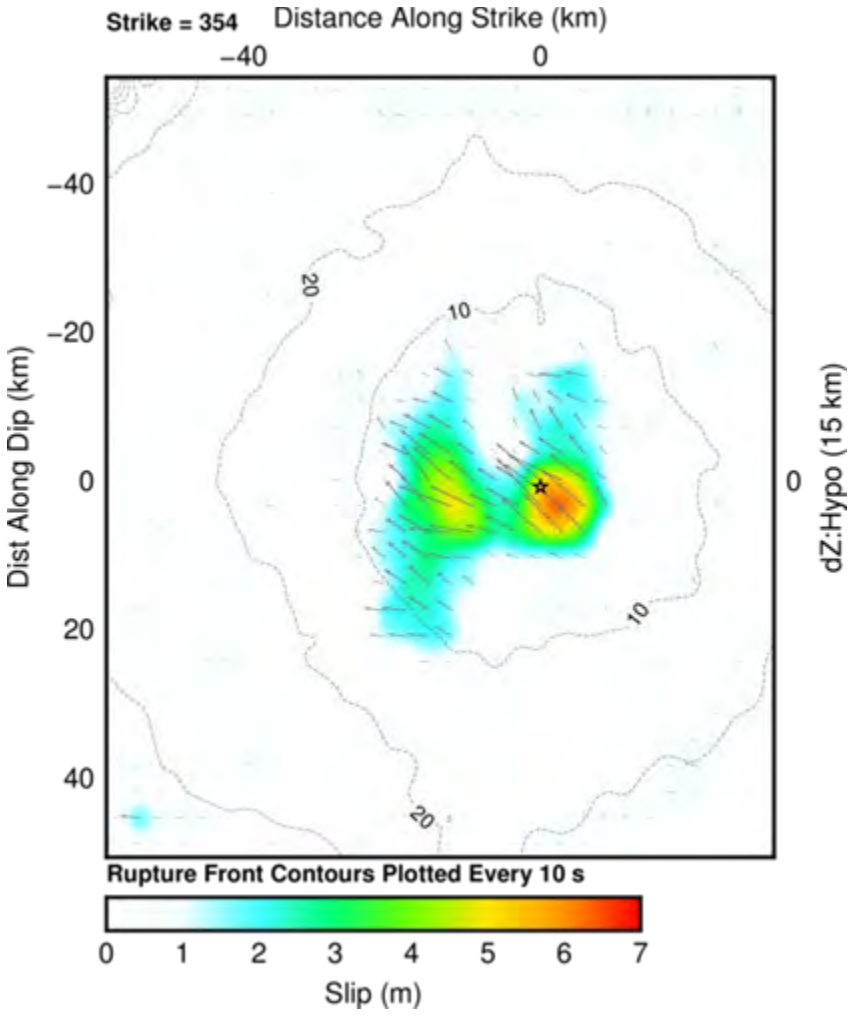

Figure 10: Finite fault inversion model from USGS. The amplitude of the slip is represented by the color spectrum and the contour lines represent the location of the wave front every 10 seconds after the initial slip.

The Coulomb 3.3 software from the USGS allows one to both calculate and visualize stresses, strains, and static displacements from a number of seismic sources, including earthquakes (Toda et al., 2011). The program utilizes the Okada model in an isotropic elastic half space in order to model geologic deformation (Okada, 1992). Several geometries were tested in order to get an ideal static model of the stress change. A receiver fault orientation with an average strike of the faults in question, 060°, as well as a rake of 180° was used for this inversion. The rake was known since the earthquake was known to be a right-lateral strike-slip fault, observed via the coseismic interferogram. The dip angle then varied in order to find the best fit for the actual event, as shown in figure 11.

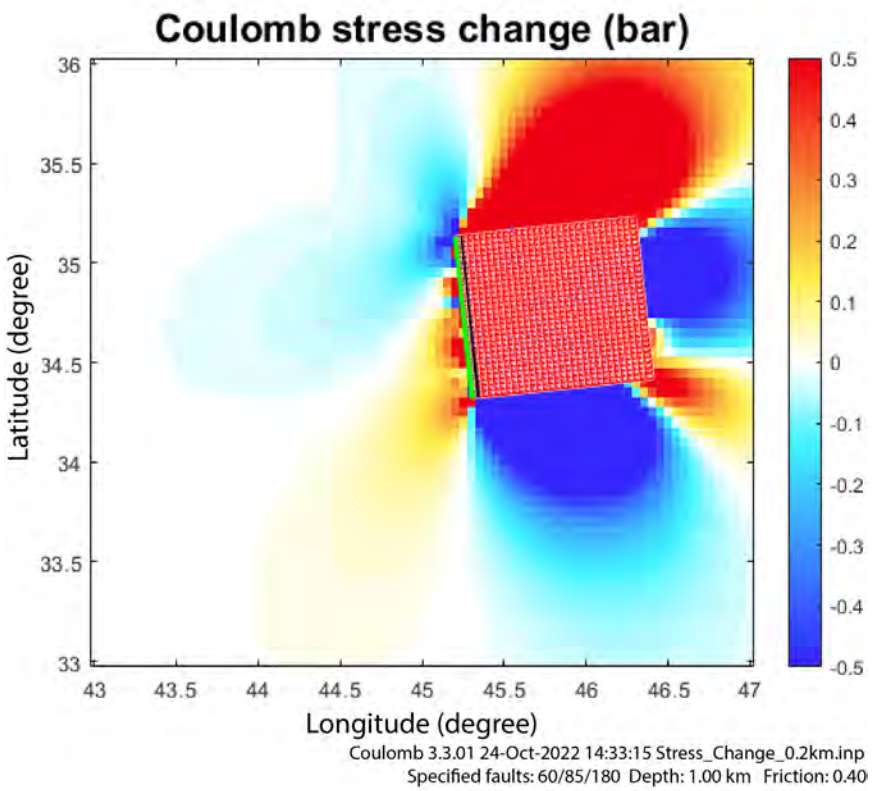

Figure 11: Static Coulomb stress change inversion with ideal fault conditions: Strike 060°, Dip 85° SE, Rake 180°. Red shows an increase in Coulomb stress and blue shows a decrease in Coulomb stress.

4.2 Dynamic Coulomb Stress Change Analysis

4.2.1 Preliminary Model Development

After analyzing the static Coulomb stress change a forward model of the dynamic stress change that resulted from the earthquake was constructed. To this end, ground displacement-time-series data from the USGS was used to analyze the ground velocity and acceleration throughout the main shock. A link to this dataset can be found in Appendix A. The dynamic modeling process was more complicated than the static modeling and was therefore broken into two portions. The first portion was the development of a coarse approximation of the model produced using fewer sources for ease of development.

This preliminary model was constructed as a first order approximation of the true propagation using the following parameters: fault area of 600 km^2, a hypocenter of 34.9° N 46.0° E and a depth of 15.0 km, these data are from the USGS moment tensor of the earthquake. Additionally, the model assumed a shear modulus of 30 GPa, which is consistent with other papers examining the 2017 event, as well as a rupture velocity of 2.6 km/s (Wang and Bürgmann, 2020). Finally, the preliminary model is divided into twenty subfaults, with the seismic moment equally divided amongst them for a coarse estimate of the propagation.

Figure 12 shows an interpolation based on the previously described forward model showing the spatial distribution of east, north, and vertical acceleration at the surface. These spatial distributions were created using code modified from Dreger and Kaverina (2000), which

is in turn based on a linear least squares method by Hartzell and Heaton (1983). While this model was simple it served a valuable purpose for the development of the final model.

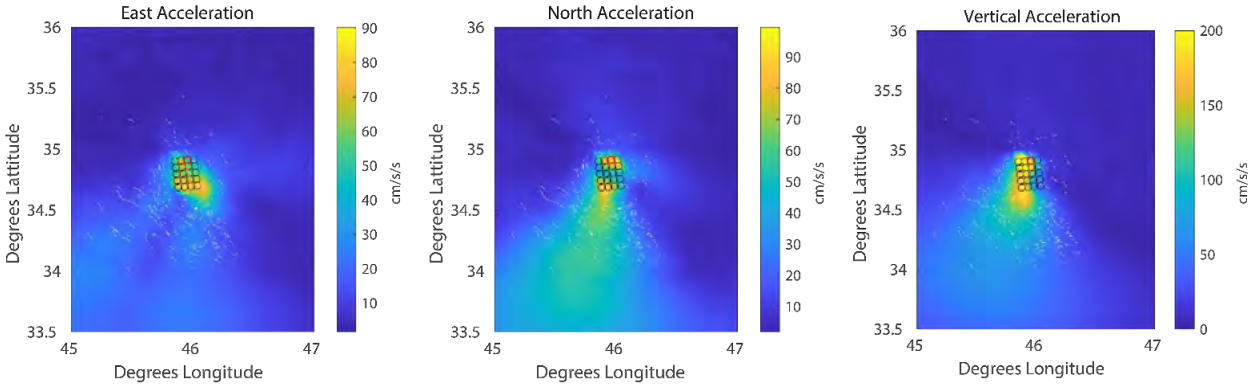

Figure 12: Simplified hypothetical models of ground motion with uniform slip. The fault plane is denoted by the array of black circles with the red circle representing the hypocenter.

4.2.2 Refinement of Model

Once the preliminary model had been developed the final phase of the study was to refine this model and analyze the results. The primary changes came in the form of a recalculated set of Green's functions and a new one-dimensional velocity profile, attained from USGS, which has a higher depth resolution at shallower depths than the previous model. A link to this velocity profile can be found in Appendix B. Additionally, the new model accounts for the heterogenous distribution of the seismic moment whereas previously it was assumed to be uniform across the fault patch. Figure 13 shows the new analysis of the data modeled in figure 12 after the model

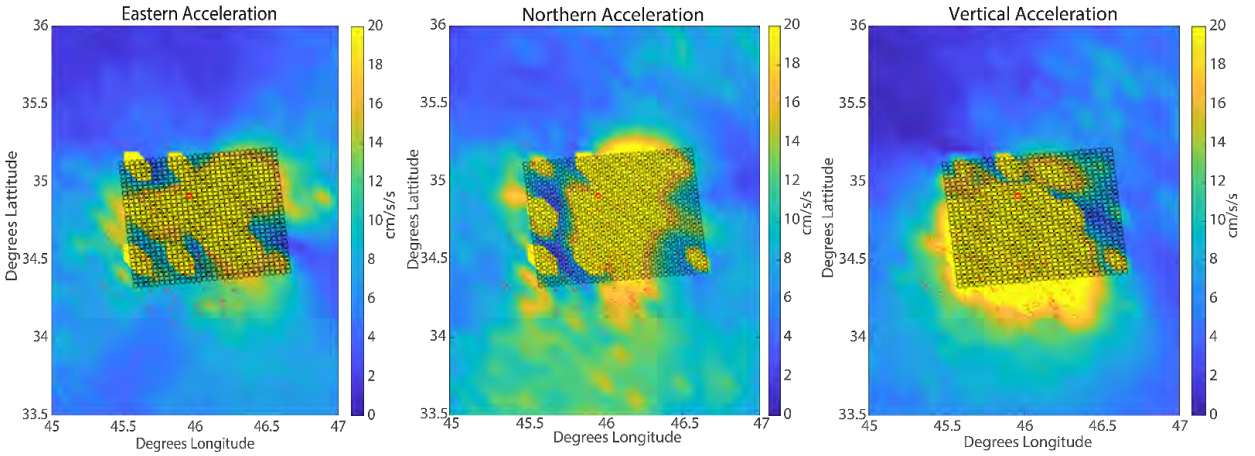

Figure 13: Recalibrated three-component acceleration figures. The leftmost figure depicts the eastward acceleration, the center figure depicts the northward acceleration, the right figure depicts the vertical acceleration. Additionally, the red lines represent the location of slip events observed by InSAR.

was run with these new parameters.

Using the same original displacement data that were used to generate the acceleration graphs. Then the first invariant of the data was calculated in order to find the peak velocity as it

is distributed spatially. Then from these velocity data the dynamic Coulomb stress change was calculated using equation 4 (Taira et al., 2018).

$$\Delta\sigma_d = \mu \frac{v_{peak}}{V_s} \tag{4}$$

Where $\Delta\sigma_d$ represents the dynamic Coulomb stress change, μ represents the shear modulus for the region, v_{peak} represents the peak ground velocity at a given point, and V_s represents the S-wave velocity of the region. The peak velocity, v_{peak}, is found using a series of three rotation tensors, thereby projecting all three components of the velocity onto a single vector. Equation 4 was then used to calculate the peak dynamic Coulomb stress change at each synthetic station. However, this new model had an issue with outlier values causing artifacts in the data. To find the appropriate seismic wavelength to trigger slip a first order Butterworth filter was applied to the simulated waveform data which made the regions of high ground acceleration easier to see. The filter was a high pass filter maxing out at 300 cm/s of velocity in order to represent the data more clearly removing points of clear statistical error in the data. Additionally, the data correlated from the three-component velocity to a single velocity vector and converted dynamic Coulomb stress as shown in figure 14 below.

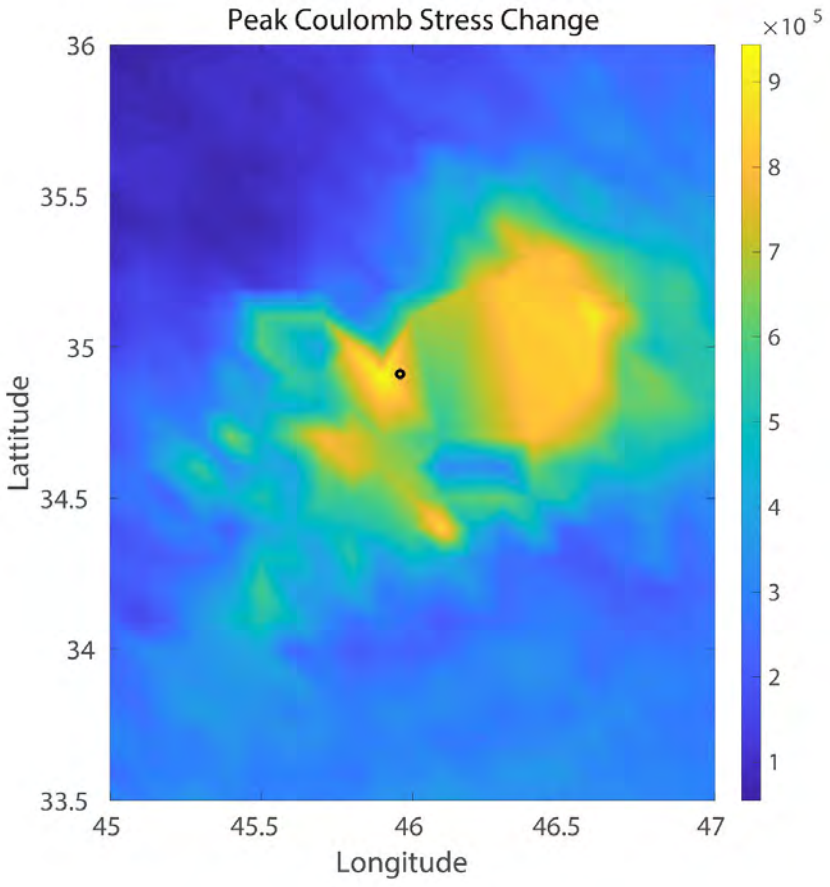

Figure 14: Peak Coulomb stress change interpolation up to 10 MPa. The epicenter of the earthquake is marked with a black circle.

5 Discussion

The data collected for both the static and dynamic Coulomb stress change associated with the main shock of the fault are inconsistent with the null hypothesis that the observed slip was not triggered by a change in the Coulomb stress in the surrounding region. As discussed previously areas where the Coulomb stress decreased are said to have been strengthened, and areas where the Coulomb stress increased are said to have been weakened. Evaluating this in relation to the fractures mapped from InSAR in figure 8 shows that most of the fractures occurred in a region that, according to its static stress change, should have become more stable as shown in figure 15 below.

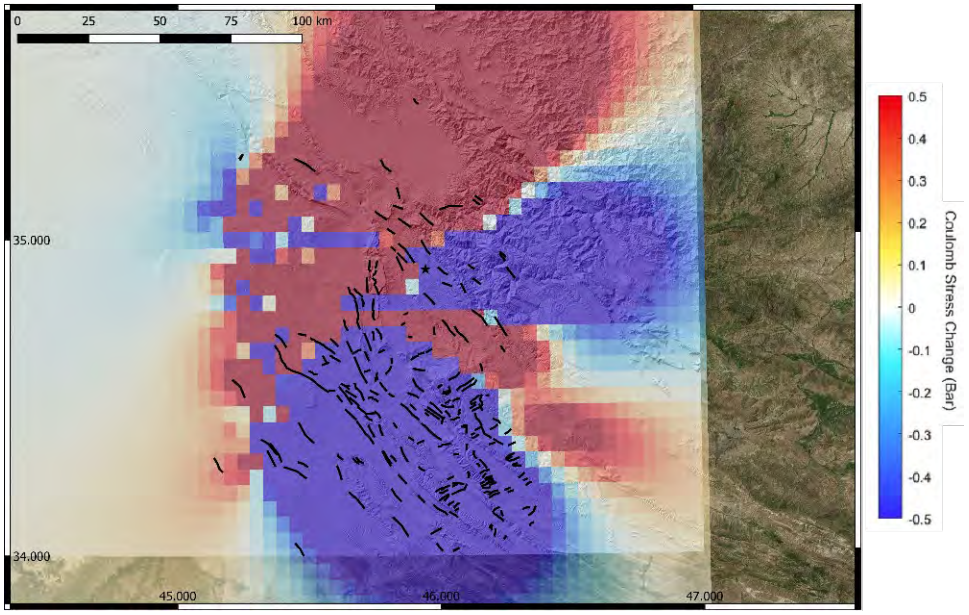

Figure 15: Coulomb stress inversion with: Strike 060°, Dip 85° SE, Rake 180° mapped onto fractures seen from InSAR on top of a digital elevation model (DEM). All of this is mapped on top of Bing VirtualEarth imagery.

The static Coulomb stress change map from the Coulomb 3.3 software was mapped onto the map of fractures using QGIS. Examination of this combined map shows the relationship between static stress and the slip pattern southeast of the epicenter. The location of the slip pattern in question is inconsistent with the first alternative hypothesis since the region in which the fractures are located was statically strengthened by the earthquake. Therefore, it is very unlikely that these fractures are due to the static stress change of the earthquake.

As shown in figure 15 the static stress change was not well spatially correlated. On the contrary, the dynamic stress changes much better spatial correlation with the areas observed to have more slip events. As shown in figure 14, the peak Coulomb stress change saw instantaneous stress changes on the order of 10 MPa to the east of the epicenter, as opposed to much lower values of around 5-6 MPa to the west. Similarly, the area southeast of the fault, by inspection, appears to have had 1-2 MPa greater of change than the area to the northwest. This strong spatial

association directly supports the second alternative hypothesis, stating that it was more likely that these triggered slips were generated by the dynamic Coulomb stress change.

In order to examine how the main shock propagated, an animation depicting the ground velocity around the area for a short time after the main shock was created. This animation serves as a visual depiction of the directivity of the earthquake. Several still images were taken from the animation and interpolated over the study region and are shown in figure 16.

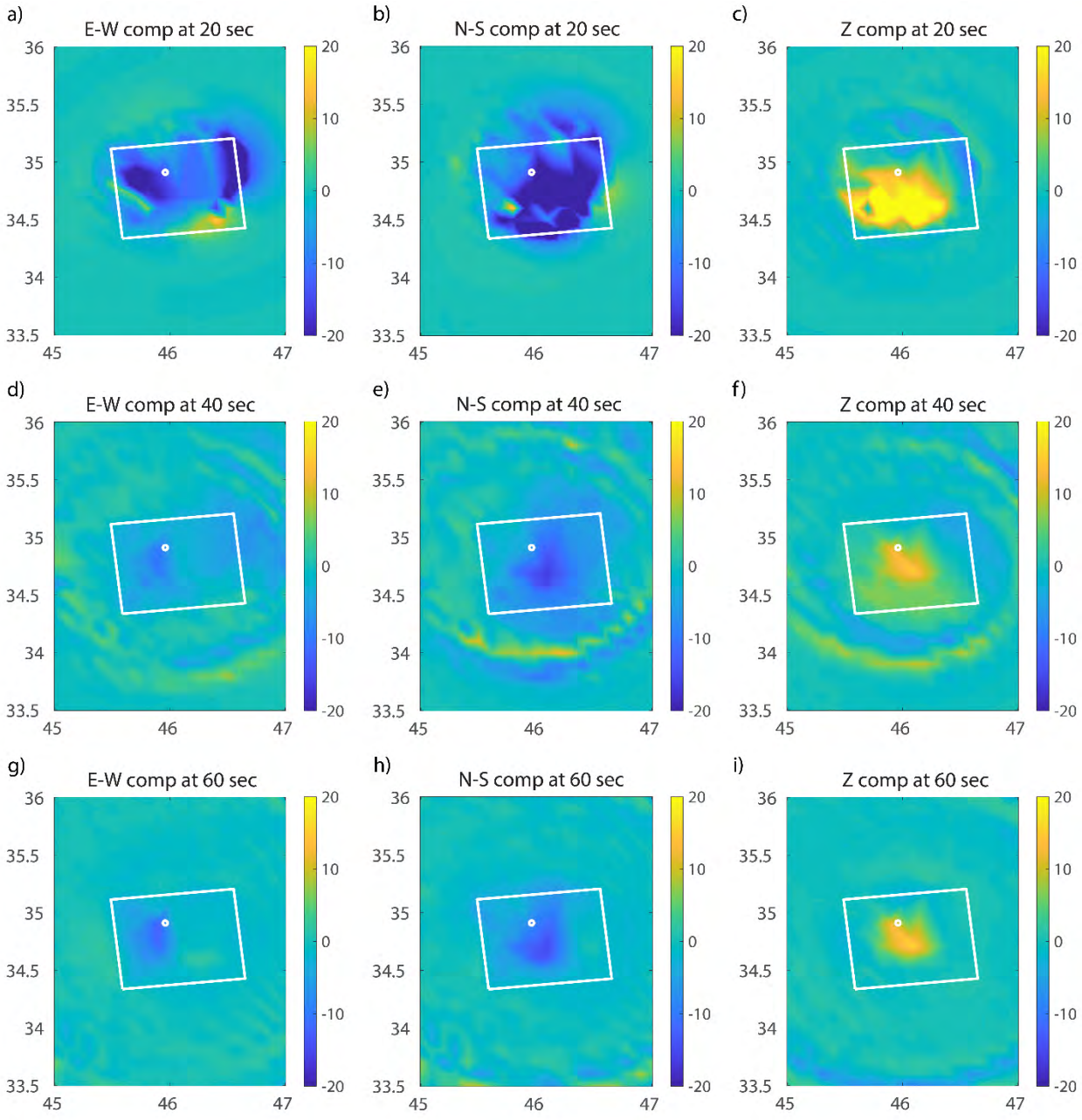

Figure 16: Images taken from an animation depicting the three-component velocity as it propagates through the system at 20, 40, and 60 seconds after the main shock. In each subplot the vertical axis represents latitude, the horizontal axis represents longitude, and the color bar ranges from -20 cm/s to 20

cm/s. For the purposes of this figure subplots a, d, and g depict east as positive. Similarly, subplots b, e, and h depict north as positive. Finally, subplots c, f, and i depict increasing altitude as positive.

As shown in figure 16, it was observed in the velocity time series data that there is a clear wavefront that has formed as the seismic energy travelled out from the hypocenter of the fault. This wavefront has a higher intensity in the southeast direction which was consistent with the higher density of observed triggered slip from InSAR observation. This is consistent with what was predicted due to the directivity of the fault propagation, with higher intensity in the direction of propagation (Grimaz, 2014). Additionally, the fact that this wavefront was observed to be equidistant from the epicenter as it propagates forward is consistent with this energy dispersion mechanism. Therefore, the three-component velocity analysis is indicative of a southeastern propagation direction of the fault slip, generating a strong directivity effect. This is concurrent with the assertion that these slips were triggered dynamically as there is clear evidence of the ground in the northwest and southeast receiving the wavefront at the same time. However, the amplitude of this wavefront was larger in the southeast direction, leading to slip being triggered at the surface.

6 Conclusions

The findings of this study have implications about the nature of triggered fault slips occurring from the main shock of an earthquake system. The clear directivity shown by the simulations is quite well spatially correlated with the areas of observed slip. This coupling of directivity and surface expression is quite telling for how earthquakes nucleate and propagate as they rupture. However, there were also some slip events that were observed outside of this zone of high dynamic Coulomb stress change, indicating that this triggering mechanism is likely not responsible for every slip seen with InSAR. This pattern of slip triggering can likely be observed in other earthquake systems and future studies will be beneficial to compare the dynamic triggering of this event with other earthquake systems.

7 Acknowledgements

I would like to thank Dr. Mong-Han Huang for being an amazing mentor to me throughout this process. It is a direct result of his guidance that I have been able to grow as not only a researcher but also as a person throughout this process. I will never forget what he has done for me throughout the time we have worked together.

I would also like to thank all of the members of the Active Tectonics Laboratory, who welcomed me into their space and helped me. I am so grateful for the warm atmosphere they have provided for me and all of the assistance they have been through this process.

Finally, I would like to thank Dr. Phillip Piccoli for coordinating the senior thesis program in the department. It is thanks to the work that he has put into this program that I have been able to have this amazing experience and for that I am quite grateful.

Bibliography:

Attema, E. P. W., Duchossois, G., & Kohlhammer, G. (1998). ERS-1/2 SAR land applications: Overview and main results. *IGARSS '98. Sensing and Managing the Environment. 1998 IEEE International Geoscience and Remote Sensing. Symposium Proceedings. (Cat. No.98CH36174)*, 1796–1798 vol.4. https://doi.org/10.1109/IGARSS.1998.703655

Barnhart, W. D., Brengman, C. M. J., Li, S., & Peterson, K. E. (2018). Ramp-flat basement structures of the Zagros Mountains inferred from co-seismic slip and afterslip of the 2017 Mw7.3 Darbandikhan, Iran/Iraq earthquake. *Earth and Planetary Science Letters*, *496*, 96–107. https://doi.org/10.1016/j.epsl.2018.05.036

Bürgmann, R., Rosen, P. A., & Fielding, E. J. (2000). Synthetic Aperture Radar Interferometry to Measure Earth's Surface Topography and Its Deformation. *Annual Review of Earth and Planetary Sciences*, *28*(1), 169–209. https://doi.org/10.1146/annurev.earth.28.1.169

Das, A., Kumar, R., & Rosen, P. (2021). Nisar Mission Overview and Updates on ISRO Science Plan. *2021 IEEE International India Geoscience and Remote Sensing Symposium (InGARSS)*, 269–272. https://doi.org/10.1109/InGARSS51564.2021.9791979

Dreger, D. & Kaverina, A. (2000). Seismic remote sensing for the earthquake source process and near-source strong shaking: a case study of the October 16, 1999 Hector Mine earthquake, *Geophysical Research Letters*, **27,** 1941–1944.

Fattahi, H., Agram, P., & Simons, M. (2017). A Network-Based Enhanced Spectral Diversity Approach for TOPS Time-Series Analysis. *IEEE Transactions on Geoscience and Remote Sensing*, 55(2), 777–786. https://doi.org/10.1109/TGRS.2016.2614925

ESRI. (2011). *National Geographic World Map* [Map]. ESRI. https://www.arcgis.com/home/item.html?id=b9b1b422198944fbbd5250b3241691b6

Grimaz, S., & Malisan, P. (2014). *Near Field Domain Effects and Their Consideration in the International and Italian Seismic Codes*. https://doi.org/10.4430/bgta0130

Gurrola, E., Sacco, G. F., Agram, P., Lavalle, M., & Rosen, P. A. (2016). *InSAR Scientific Computing Environment (ISCE): An Earth Science SAR Processing Framework, Toolbox, and Foundry*. 25.

Hartzell, S.H. & Heaton, T.H. (1983). Inversion of strong ground motion and teleseismic waveform data for the fault rupture history of the 1979 Imperial Valley, California, earthquake, *Bulletin of the Seismological Society of America*, 73, 1553– 1583

Kilb, D., Gomberg, J., & Bodin, P. (2002). Aftershock triggering by complete Coulomb stress changes: aftershock triggering by coulomb stress changes. *Journal of Geophysical Research: Solid Earth*, *107*(B4), ESE 2-1-ESE 2-14. https://doi.org/10.1029/2001JB000202

King, G. C. P., Stein, R. S., & Lin, J. (1994). *Static Stress Changes and the Triggering of Earthquakes*. 19.

Massonnet, D., Rossi, M., Carmona, C., Adragna, F., Peltzer, G., Feigl, K., & Rabaute, T. (1993). The displacement field of the Landers earthquake mapped by radar interferometry. *Nature*, *364*(6433), 138–142. https://doi.org/10.1038/364138a0

Nandan, S., Ouillon, G., & Sornette, D. (2022). Are Large Earthquakes Preferentially Triggered by Other Large Events? *Journal of Geophysical Research: Solid Earth*, 127(8). https://doi.org/10.1029/2022JB024380

Nissen, E., Elliott, J. R., Sloan, R. A., Craig, T. J., Funning, G. J., Hutko, A., Parsons, B. E., & Wright, T. J. (2016). Limitations of rupture forecasting exposed by instantaneously triggered earthquake doublet. *Nature Geoscience*, *9*(4), 330–336. https://doi.org/10.1038/ngeo2653

Okada, Y. (1992). Internal deformation due to shear and tensile faults in a half-space. *Bulletin of the Seismological Society of America*, *82*(2), 1018–1040. https://doi.org/10.1785/BSSA0820021018

Price, E. J., & Sandwell, D. T. (1998). Small-scale deformations associated with the 1992 Landers, California, earthquake mapped by synthetic aperture radar interferometry phase gradients. *Journal of Geophysical Research: Solid Earth*, *103*(B11), 27001–27016. https://doi.org/10.1029/98JB01821

Rosen, P. A., Hensley, S., Joughin, I. R., Li, F. K., Madsen, S. N., Rodríguez, E., & Goldstein, R. M. (2000). Synthetic Aperture Radar Interferometry. *Proceedings of the IEEE*, 88(3), 50.

Simons, M., & Rosen, P. A. (2015). Interferometric Synthetic Aperture Radar Geodesy. In *Treatise on Geophysics* (pp. 339–385). Elsevier. https://doi.org/10.1016/B978-0-444-53802-4.00061-0

Toda, S., Stein, R.S., Sevilgen, V., and Lin, J., (2011), Coulomb 3.3 Graphic-rich deformation and stress-change software for earthquake, tectonic, and volcano research and teaching—user guide: U.S. Geological Survey Open-File Report 2011–1060, 63 p., available at https://pubs.usgs.gov/of/2011/1060/.

Taira, T., Nayak, A., Brenguier, F., & Manga, M. (2018). Monitoring reservoir response to earthquakes and fluid extraction, Salton Sea geothermal field, California. *Science Advances*, *4*(1), e1701536. https://doi.org/10.1126/sciadv.1701536

Wallace, L. M., Kaneko, Y., Hreinsdóttir, S., Hamling, I., Peng, Z., Bartlow, N., D'Anastasio, E., & Fry, B. (2017). Large-scale dynamic triggering of shallow slow slip enhanced by overlying sedimentary wedge. *Nature Geoscience*, *10*(10), 765–770. https://doi.org/10.1038/ngeo3021

Wang, K., & Bürgmann, R. (2020). Probing Fault Frictional Properties During Afterslip Updip and Downdip of the 2017 *Mw* 7.3 Sarpol-e Zahab Earthquake With Space Geodesy. *Journal of Geophysical Research: Solid Earth*, *125*(11). https://doi.org/10.1029/2020JB020319

Zebker, H. A., & Goldstein, R. M. (1986). Topographic mapping from interferometric synthetic aperture radar observations. *Journal of Geophysical Research*, *91*(B5), 4993. https://doi.org/10.1029/JB091iB05p04993

Honor code:

I pledge on my honor that I have not given or received any unauthorized assistance or plagiarized on this assignment.

Appendix A: USGS Coulomb 3.3 Dataset

https://earthquake.usgs.gov/product/finite-fault/us2000bmcg/us/1539813246562/coulomb.inp

Appendix B: USGS Finite Fault Inversion

https://earthquake.usgs.gov/product/finite-fault/us2000bmcg/us/1539813246562/complete_inversion.fsp